Journal of The Electrochemical Society





# Highly Conducting *Bombyx mori* Silk Fibroin-Based Electrolytes Incorporating Glycerol, Dimethyl Sulfoxide and [Bmim]$PF_6$

*Journal of The Electrochemical Society*, 2020 **167** 070551

# Highly Conducting *Bombyx mori* Silk Fibroin-Based Electrolytes Incorporating Glycerol, Dimethyl Sulfoxide and [Bmim]$PF_6$

**Tânia C. D. Fernandes,[1] Helena M. R. Rodrigues,[2,3] Filipe A. A. Paz,[4] Joana F. M. Sousa,[5] Artur J. M. Valente,[5] Maria M. Silva,[1] Verónica de Zea Bermudez,[2,z] and Rui F. P. Pereira[1,z]**

[1]*Chemistry Center and Chemistry Department, University of Minho, Campus de Gualtar, 4710-057 Braga, Portugal*
[2]*Chemistry Department and CQ-VR, University of Trás-os-Montes e Alto Douro, Apartado 1013, 5001-801 Vila Real Codex, Portugal*
[3]*REQUIMTE, Instituto Superior de Engenharia do Porto, 4200-072 Porto, Portugal*
[4]*Chemistry Department, University of Aveiro, CICECO-Aveiro Institute of Materials, 3810-193 Aveiro, Portugal*
[5]*Chemistry Department, University of Coimbra, 3004-535 Coimbra, Portugal*

Green, transparent and flexible electrolyte films composed of a *Bombyx mori* silk fibroin (SF) host biopolymer doped with glycerol (G), dimethyl sulfoxide (DMSO, D) and 1-butyl-3-methylimidazolium hexafluorophosphate ([Bmim]$PF_6$) ionic liquid (IL), were synthesized. The materials were represented by the notation SF@GD@$IL_x$ (x = 15, 20 and 30 is the mass ratio of SF/[Bmim]$PF_6$ in %). SF@, SF@G, SF@D and SF@GD samples were also prepared. DMSO was found to play a dual-role, acting as solvent of [Bmim]$PF_6$, and enhancing ionic conductivity. DMSO, alone or combined with [Bmim]$PF_6$, led to the increase of the mean roughness and induced the formation of more ordered Silk II conformations ($\beta$-sheets). No structural modifications were detected in the SF@GD@$IL_x$ samples upon increasing the temperature up to 100 °C. The highest ionic conductivity was exhibited by the IL-rich sample SF@GD@$IL_{30}$ (1.07 and 4.61 mS $cm^{-1}$, at 22 and 100 °C, respectively). In the [Bmim]$PF_6$-doped electrolytes "free" and coordinated $PF_6^-$ ions coexist. The weight losses occurring below 200 °C involved essentially the release of adsorbed water and DMSO. The suitable mechanical properties, high ionic conductivity and good electrochemical stability suggest that these electrolytes are attractive candidates for application in electrochemical devices.
 [DOI: 10.1149/1945-7111/ab8313]

Manuscript submitted January 29, 2020; revised manuscript received February 26, 2020. Published April 6, 2020. *JES Focus Issue on Challenges in Novel Electrolytes, Organic Materials, and Innovative Chemistries for Batteries in Honor of Michel Armand.*

Polymer electrolytes (PEs), essentially composed of a host polymer bearing electron-donor atoms (poly(oxyethylene) being the gold standard) and a guest ionic salt, have not ceased to attract the community of solid state electrochemistry in the last 40 years. These systems offer several attractive features, in particular good electrochemical properties, low cost, high safety, reduction of problems associated with environmental issues, elimination of electrolyte leakage problems, and good flexibility. PEs may also act as separators, adhesives and cell sealants in electrochemical devices. Their technological impact spans a wide variety of applications, ranging from electrochromic windows and displays, fuel cells, sensors, and dye-sensitized solar cells, to supercapacitors and high energy density rechargeable batteries.

The advent of solid (or "dry") PEs (SPEs), introduced by Armand,[1,2] provided an attractive alternative to non-aqueous liquid electrolytes in light-weight, rechargeable lithium batteries.[3] SPEs suffered from a series of shortcomings that delayed their application in commercial devices. These included a marked tendency to crystallize, significantly lower ionic conductivity (usually lower than $10^{-5}$ S $cm^{-1}$ at room temperature) than non-aqueous liquid electrolytes, and a great tendency for exhibiting salting-out effects at high salt concentration. Several possibilities have been exploited through the years in terms of polymer architecture and salt design to enhance ionic conductivity. Reports of innovative PEs with improved performance are being published regularly.[4] The incorporation of additives (plasticizers) into PEs was recognized as an alternative strategy, leading to the development of the so-called "hybrid" PEs or, in some cases, the gel PEs (GPEs).[5,6] Recently the huge potential offered by ionic liquids (ILs), both as solvents and electrolytes, prompted researchers to include them in PEs as well.[7,8]

In the last decades, fossil-fuel depletion, increasing concentration of greenhouse gases, and uneven distribution of energy sources have driven the quest for cleaner, safer, cheaper, and more efficient energy materials and devices. This transition to a greener energy scenario, probably the greatest technological challenge of this century, has obvious implications in climate, economic development, and humankind progress. The United Nations launched at the global scale the *Sustainable Development Goals*, which are the blueprint to ensure universal access to affordable, reliable, sustainable and modern energy by 2030.[9]

With these concerns in mind, a part of the community of PEs turned its attention to natural polymers. On account of their abundance, easy, fast and clean synthesis, and eco-friendly and biodegradable properties, polysaccharides emerged as potential candidates as host macromolecules for the development of a new generation of PEs.[10] Systems based on corn starch,[11] cellulose,[12,13] agar,[14,15] k-carrageenan,[16–18] and chondroitin sulphate[19] were proposed.

The number of protein-based PEs composed reported in the literature is, however, rather scarce. Deoxyribonucleic acid (DNA)[20] and gelatin[21,22] were investigated. Recently some of us were attracted by the extraordinary features of silkworm silk[23]: outstanding mechanical properties (high tensile strength and great extensibility), controllable biodegradability, heat-conducting ability, wide optical window, non-toxicity, biocompatibility, and easy processing into films.

Silks are spun by several arthropods (e.g., silkworms, spiders, scorpions, mites, bees and flies). The most extensively produced and employed silk, which has a tradition of more than 5000 years in the textile industry, is that obtained from the cocoons spun by the silkworm of the domesticated *Bombyx mori* moth. The thread of silkworm silk fibers comprises a core fibrous protein (silk fibroin (SF)) which is surrounded by a glue-like protein (silk sericin (SS)).[23]

[z]E-mail: vbermude@utad.pt; rpereira@quimica.uminho.pt

SF, the most widely employed, is an aqueous insoluble high molecular weight (200–350 kDa or more) protein containing more than 5000 amino acids. Degumming is the process of removing SS from silk fibers to obtain pure SF.

In the last few years, the range of potential applications of SF fibers has been enlarged to several high-tech areas. Exciting new applications have been proposed in the field of energy, targeting the bio-inspired use of SF in electrochromic devices,[24] electromechanical actuators,[25] and batteries.[26–30]

The controlled evaporation of water from an aqueous solution of SF leads to protein self-assembly and to the consequent formation of a film with a series of properties which are particularly appealing if applications as electrolytes are envisaged: high transparency, mechanical robustness, high surface flatness, controlled thickness, biocompatibility, or biodegradation.[24,31,32] These properties can be tuned or new ones can even be activated through doping the original aqueous SF solution with organic and/or inorganic molecules.[24,31,32] At room temperature a non-doped SF film exhibits some brittle character and extremely low ionic conductivity. To circumvent both drawbacks some of us[24] introduced two electrolytes composed of SF, glycerol, acting as a plasticizer, and a lithium salt (lithium bis (trifluoromethanesulfonyl) imide (LiTFSI) and lithium tetrafluoroborate ($LiBF_4$)). At room temperature, the resulting electrolytes exhibited poor ionic conductivity ($1.06 \times 10^{-9}$ and $1.13 \times 10^{-9}$ S cm$^{-1}$, respectively). Although these values were about three orders of magnitude higher than that displayed by the non-doped SF film ($3.71 \times 10^{-12}$ S cm$^{-1}$ at 23 °C), they were still far from the threshold value that allows foreseeing any practical applications in batteries (i.e. $10^{-5}$ S cm$^{-1}$); however, they were acceptable to guarantee the operation of electrochromic devices.[24]

In the present work, seeking the preparation of improved SF-based electrolytes with significantly higher ionic conductivity levels, we decided to replace in the above formulation the ionic salt by an IL. The IL chosen was 1-butyl-3-methylimidazolium hexafluorophosphate ([Bmim]$PF_6$). At room temperature this hydrophobic, green compound exhibits high ionic conductivity (0.46 S cm$^{-1}$ at 25 °C)[33] and a broad electrochemical stability domain (5.95 V at ambient conditions, using a gold (Au) rotating disk electrode and platinum as a quasi-reference electrode[33]). [Bmim]$PF_6$ is insoluble in water, but easily dissolved in DMSO. The use of the latter solvent seemed particularly attractive for the development of PEs. Aprotic DMSO is considered a green solvent for inorganic/organic materials. Indeed, on account of its very low toxicity, it has been extensively used in biomedicine. This organosulfur compound has several additional advantages, such as low viscosity and volatility, and high resistance to redox reactions. It may also exert a plasticizing effect.[34] From the chemical standpoint, DMSO is an appealing solvent with high dielectric constant ($\varepsilon_{20\ °C} = 46.68$), dipolar moment ($\mu_{25\ °C} = 4.1$ D), and polarity index (10.2), and a remarkably high donor number (DN = 29.8 kcal mol$^{-1}$).[35] Owing to these attributes DMSO has been widely explored in the field of materials for advanced batteries.[36–45]

Herein, innovative electrolytes containing SF, glycerol, DMSO and [Bmim]$PF_6$, noted as SF@GD@$IL_x$, where x = 15, 20 and 30 is the mass ratio of SF/[Bmim]$PF_6$ in %, were synthesized. In an attempt to determine the influence of each component, four blank samples were also prepared: a non-doped SF film, a SF film doped exclusively with glycerol, a SF film doped exclusively with DMSO, and a SF film doped with a mixture of glycerol and DMSO. For the sake of clarity, these samples will be henceforth denoted as SF@, SF@G, SF@D, and SF@GD, respectively. The morphological, structural, thermal, and electrochemical properties of the as-obtained electrolytes were studied in depth.

## Experimental

***Materials.—****Bombyx mori* cocoons were supplied by APPACDM from Castelo Branco (Portugal). Sodium carbonate (99.5%, $Na_2CO_3$, Sigma-Aldrich) and lithium bromide (≥99%, LiBr, Sigma-Aldrich) were used as received. Slide-A-Lyzer™ G2 dialysis cassettes (molecular-weight cutoff of 3.5 kDa) were purchased from Thermo Fisher Scientific. All aqueous solutions were prepared using ultrapure water. Glycerol (99.5%, Himedia), dimethyl sulfoxide (DMSO) (99.99%, Fisher Scientific) and 1-butyl-3-methylimidazolium hexafluorophosphate ([Bmim]$PF_6$) (99.9%, Solvionic) were used as received, and stored in a dry argon-filled glove box.

***Preparation of SF aqueous solution.—***For degumming (removal of SS from the *Bombyx mori* cocoons and isolation of SF), cocoons were cut into small pieces and boiled in a 0.02 M $Na_2CO_3$ solution for exactly 30 min. The fibers were then rinsed several times with distilled water, squeezed out to remove the excess water, and finally dried overnight in a fume hood at 60 °C. The as-obtained SF fibers were dissolved in a 9.3 M LiBr solution at 60 °C for 4 h. The solution was subsequently dialyzed against ultrapure water until complete salt removal dialysis cassettes. The efficiency of the dialysis process was monitored by conductivity measurements. To remove impurities, SF aqueous solution was centrifuged twice at 5000 rpm at 4 °C for 30 min. The final concentration of SF (7.4 w/v %) was determined by measuring the dry weight of the solution. The resultant SF solution was stored at 4 °C until further use.

***Synthesis of the electrolytes.—***The SF-based electrolytes were prepared following the following procedure. A volume of 2 ml of the prepared SF aqueous solution was mixed with glycerol (20 w/w % glycerol/SF). In parallel, [Bmim]$PF_6$ was dissolved in 300 $\mu$l of DMSO and then added, under continuous stirring, to the mixture of SF aqueous solution and glycerol. The electrolyte films were produced by casting the mixtures onto poly(propylene) Petri dishes and dried in a fume hood at 30 °C for 72 h. The detailed composition of the electrolytes can be found in Table SI.

## Characterization Techniques

The ionic conductivity ($\sigma_i$) of the electrolytes was measured using an Autlab PGSTAT-12 (Eco Chemie) equipment. The SF-based films were placed between two Au blocking electrodes, and complex impedance spectroscopy measurements were carried out, at frequencies between 1 MHz and 65 kHz, with an amplitude of 10 mV. The electrode/electrolyte/electrode assembly was secured in a suitable constant volume support and installed in a Buchi TO51 tube oven with a K-type thermocouple placed close to electrodes to control temperature. Bulk conductivities were obtained during heating cycles (room temperature to 100 °C) with temperature intervals of approximately 10 °C. The ionic conductivity of the samples was determined using the equation

$$\sigma_i = \frac{d}{R_b \times A} \quad [1]$$

where $d$ is the thickness, $R_b$ is the bulk resistance, and $A$ is the area of the electrolyte.

The electrochemical stability window of electrolytes was evaluated under an argon atmosphere using a two-electrode cell configuration as described elsewhere.[14] Briefly, a 25 $\mu$m diameter Au microelectrode surface was polished (moist cloth and 0.05 $\mu$m alumina powder—Buehler, Spain) outside the glove box. The cell was assembled by locating a clean lithium (Li) disk counter electrode (99.9%, 19 mm diameter, 0.75 mm thick, Aldrich,) on a stainless-steel current collector, and centering the electrolyte on the electrode surface. An Autolab PGSTAT-12 (Eco Chemie, England) was used to record voltammograms between −2.0 to + 5.0 V and a scan rate of 500 mV s$^{-1}$. Measurements were performed at room temperature, within a Faraday cage.

Differential Scanning Calorimetry (DSC,) analysis was performed using a Mettler Toledo DSC 821e equipment. The electrolytes were sealed in standard 40 $\mu$l aluminum crucibles and the thermograms were acquired from 25 to 350 °C at a rate of 10 °C min$^{-1}$, under argon purge (flow rate of 10 ml min$^{-1}$).

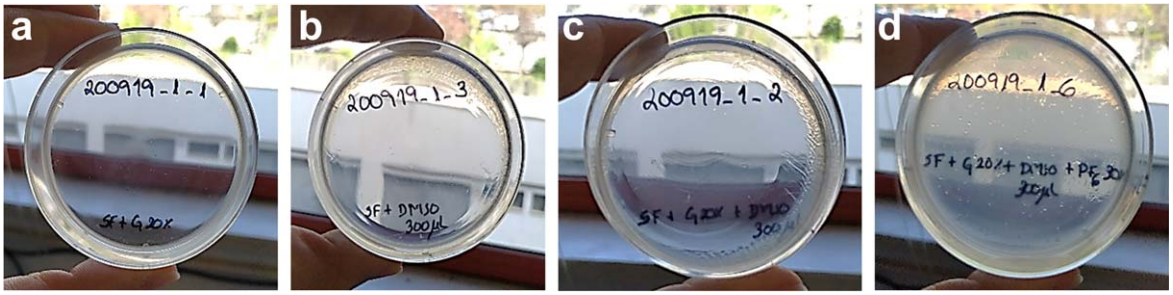


**Figure 1.** Physical appearance of the (a) SF@G, (b) SF@D, (c) SF@GD and (d) SF@GD@$IL_{30\%}$ electrolytes.

Thermal Gravimetric Analysis (TGA) of the electrolytes were obtained in a TG 209 F3 Tarsus thermogravimetric analyzer (Netzsch Instruments). Samples (ca. 5 mg) were weighed in alumina pans and heated from 30 to 600 °C, at 10 °C $min^{-1}$ under nitrogen atmosphere (flow rate of 20 ml $min^{-1}$).

A Shimadzu UV/Vis 2450 spectrometer was used to record the ultraviolet/visible (UV-vis) spectra of the electrolytes in the 200–800 nm range, with a bandwidth of 1.0 nm.

Attenuated Total Reflectance (ATR)/Fourier Transform Infrared (FT-IR) spectra of the electrolytes were recorded in an IRAffinity 1 s Fourier Transform Infrared Spectrophotometer—Shimadzu, equipped with a diamond crystal. Prior to measurement, a small piece of each sample was transferred to the diamond crystal and pressed. The spectra were recorded at room temperature in the 4000–400 $cm^{-1}$ range by averaging 64 scans and a resolution of 4 $cm^{-1}$ using the LabSolutions IR software.

High Resolution Scanning Electronic Microscopy (HR-SEM) micrographs were obtained at 3.0 kV using a FEI Quanta 650 FEG microscope. Elemental mapping analysis was performed by Energy Dispersive X-ray Spectroscopy (EDS) using an Inca Energy 350 system (Oxford Instruments). The acquisition time for each EDS spectrum was 15 min.

AFM analysis was performed in an AFM CSI Nano-Observer equipment (Scientec) in tapping mode using a super sharp Si HQ: NSC19/FORTA probe with a frequency resonance of 60 kHz and a spring constant of 0.3 N $m^{-1}$. In order to improve the images quality flattening and elimination of line noise tools were applied using the Gwyddion 2.54 software. Since the films were quite thin and it was likely that during the drying process the film surface in direct contact with the mold would mimic its indentations, the AFM analysis was performed in the area that was left to dry in air. Prior to each measurement the film surface was briefly exposed to a nitrogen gas flow to remove any dust or fibers that could have deposited on the surface during the drying process. Moreover, due to the film thickness, it was necessary to guarantee that the double tap glue used to immobilize the film on the AFM support was perfectly homogenous, and devoid of any air bubbles that might interfere with the measurement. Each film was analyzed in different areas. The images acquired and reported here were found to be representative for each sample.

Water static contact angle (CA) measurements were performed using the sessile drop method. Experiments were performed in a temperature-controlled chamber at 25 ± 1 °C using a Krüss DSA25S drop shape analyzer controlled by the software ADVANCE. The volume of the liquid droplets was kept constant (5 $\mu$l). Contact angles were determined from digital images acquired by a video camera using the Young–Laplace fitting. The CA values were measured in at least 5 different spots in each film. CA values correspond to the average of all the measurements and the error corresponds to the arithmetic mean of the root mean square error.

Powder X-ray Diffraction (PXRD) data for the materials were collected at ambient temperature on an Empyrean PANalytical diffractometer (Cu $K_{\alpha 1,2}$ X-radiation, $\lambda_1$ = 1.540598 Å; $\lambda_2$ = 1.544426 Å), equipped with an PIXcel 1D detector and with the sealed tube operating at 45 kV and 40 mA. Data were collected in transmission mode using the provided Empyrean reflection-transmission spinner by positioning the samples in-between two transparent acetate foils purchased from STOE & Cie GmbH (Darmstadt) so to ensure the lowest possible background. Intensity data were collected by the step-counting method (step 0.01°), in continuous mode, in the ca. $3.5 \leqslant 2\theta \leqslant 50°$ range.

Variable-temperature PXRD data were collected on a PANalytical X'Pert Powder diffractometer Cu $K_{\alpha 1,2}$ X-radiation ($\lambda_1$ = 1.540598 Å; $\lambda_2$ = 1.544426 Å) under an air atmosphere, equipped with a PIXcel 1D detector, a flat-plate sample holder in a Bragg-Brentano para-focusing optics configuration (40 kV, 50 mA), and a high-temperature Anton Paar HKL 16 chamber controlled by an Anton Paar 100 TCU unit. Intensity data were collected in the continuous mode (ca. 100 s data acquisition) in the angular range ca. $5 \leqslant 2\theta° \leqslant 35$.

## Results and Discussion

The visual observation of the SF@G, SF@D, SF@GD and SF@GD@$IL_{30\%}$ electrolyte films (Fig. 1) suggested that, while the incorporation of glycerol, DMSO or the mixture of both compounds into SF did not exert any dramatic influence on the transparency of the materials, the addition of the IL led to a significant decrease of the transmittance (T). These conclusions were confirmed in the UV–vis spectra shown in Fig. 2 which reveal that, while glycerol exerted a negligible effect ($\Delta T = 1.7\%$, at 550 nm), DMSO merely induced a slight decrease of T ($\Delta T = 4.2\%$, at 550 nm), taking the T of SF@ as reference. In contrast the presence of $[Bmim]PF_6$ caused a dramatic effect on the transparency of the films ($\Delta T = 37.5\%$, at 550 nm, for SF@GD@$IL_{30\%}$) (Fig. 2).

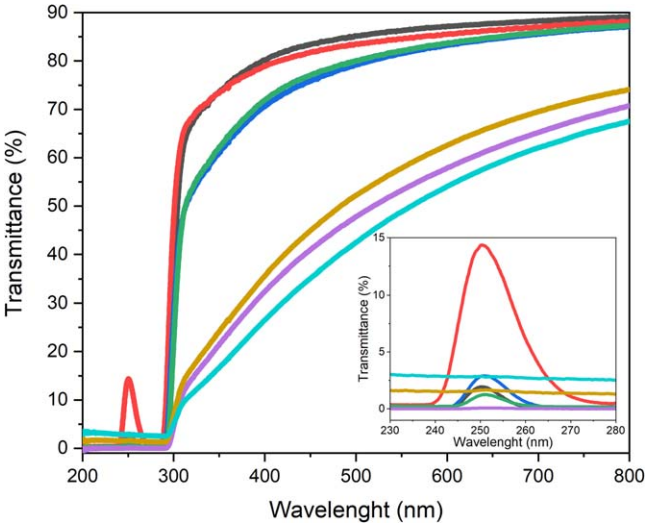


**Figure 2.** UV–vis spectra of the SF@ (black line), SF@G (red line), SF@D (green line), SF@GD (blue line), SF@GD@$IL_{15\%}$ (violet line), SF@GD@$IL_{20\%}$ (dark yellow line) and SF@GD@$IL_{30\%}$ (cyanide line) electrolytes in the 200–800 nm region.

The UV–vis spectrum of the SF@ film displays an absorption band in the mid-UV region at 250 nm (Fig. 2), which can be assigned to the $\pi \rightarrow \pi^*$ transition occurring in some aromatic amino acids (tyrosine, phenylalanine and tryptophan—Fig. S1 is available online at stacks.iop.org/JES/167/070551/mmedia) present in the SF chain.[46–48] Glycerol boosted the intensity of this band, but DMSO had the opposite effect. Upon addition of [Bmim]$PF_6$, the complete quenching of this band was observed, indicating an effective interaction between the IL and the SF chains.

The HR-SEM images (Figs. 3a–3g, Figs. S2–S3) reveal that the texture of the electrolytes doped with glycerol (Fig. 3b), DMSO (Fig. 3c) or a mixture of both these compounds (Fig. 3d) are homogeneous and practically identical to that of the non-doped sample (Fig. 3a). HR-SEM images recorded at higher magnification demonstrated, however, that SF@G exhibited a slightly more irregular texture than SF@ (Fig. S2). This finding can be attributed to the aggregation of the redundant glycerol molecules.[49]

Close analysis of the HR-SEM images shown in Figs. 3e–3g allows inferring that the electrolytes incorporating [Bmim]$PF_6$ preserved the texture of SF@. Unlike the HR-SEM images obtained for the samples devoid of IL (Figs. 3a–3d), the HR-SEM images recorded for the [Bmim]$PF_6$-doped materials exhibit lighter areas, the density of which is a function of the IL concentration. To check if the existence of these areas was associated with [Bmim]$PF_6$–rich regions, EDS analyses were performed to identify the distribution of relevant elements in the SF@GD@$IL_x$ samples: carbon (C), oxygen (O), and nitrogen (N) atoms in the SF chains; C and N atoms in the imidazolium cations; and phosphorous (P) and fluorine (F) atoms in the $PF_6^-$ anions. Surprisingly the EDS mapping images deduced for the darker and lighter regions of a selected area of the HR-SEM image of SF@GD@$IL_{30\%}$ did not reveal any noteworthy differences in terms of chemical composition (Figs. 3h, 3i). Although it is clear that the lighter regions must be somehow related with the presence of the IL, we suspect that they might have been formed upon irradiation of these samples during the measurement. At present, without any other piece of evidence, we prefer to leave their origin unknown.

To get insight into the topographical alterations induced by the addition of each dopant on SF, an AFM analysis was performed. Figures 4a and 4b (left axis) led us to conclude that the addition of glycerol to SF introduced a visible decrease in the film mean roughness (from 16.56 ± 1.48 nm (SF@) to 10.35 ± 2.44 nm (SF@G)). In contrast the addition of DMSO, of the glycerol +DMSO mixture, and of the growing concentration of [Bmim]$PF_6$, resulted in a gradual increase of the mean roughness in spite of the presence of glycerol (Figs. 4a and 4b (left axis)). These findings clearly show that chemical change introduced on SF (i.e., the incorporation of the three different chemical compounds) had a significant impact on the physical properties of the surface. In the case of pristine SF@, as water evaporated and the SF solution became more concentrated, the increase in the molecular mobility of the chains probably promoted the occurrence of globular structures.[50] Upon addition of glycerol, the surface of the SF@G film became smoother, suggesting that this plasticizer inhibited the above process presumably because of the formation of hydrogen bonds between the SF chains and glycerol. In contrast, the incorporation of exclusively DMSO, of the glycerol+DMSO mixture or of the glycerol+DMSO+[Bmim]$PF_6$ mixture caused the opposite effect, increasing progressively the roughness of the electrolyte films. These observations indicated that the role played by DMSO and the IL might be similar to that of methanol, which is known to induce the increase of the crystallinity of the silk fibers, and ultimately to changes in the surface topography. We will return to this aspect in the discussion of the XRD data.

The conclusions retrieved from AFM data prompted us to check if the marked changes observed in the surface topography were

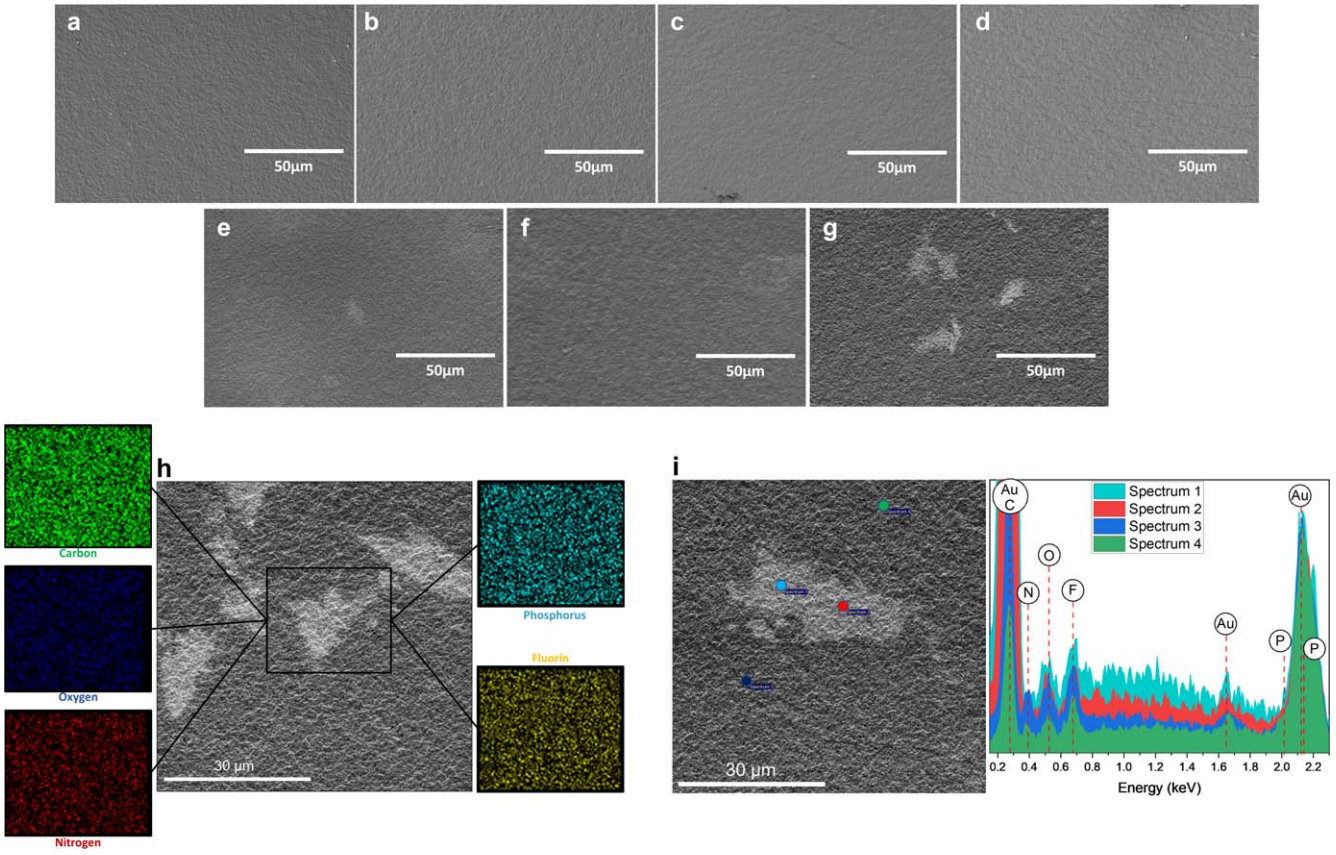


**Figure 3.** A: HR-SEM images of the (a) SF@, (b) SF@G, (c) SF@D, (d) SF@GD, (e) SF@GD@$IL_{15\%}$, (f) SF@GD@$IL_{20\%}$ and (g) SF@GD@$IL_{30\%}$ electrolytes. (h) and (i): EDS mapping images of SF@GD@$IL_{30\%}$.

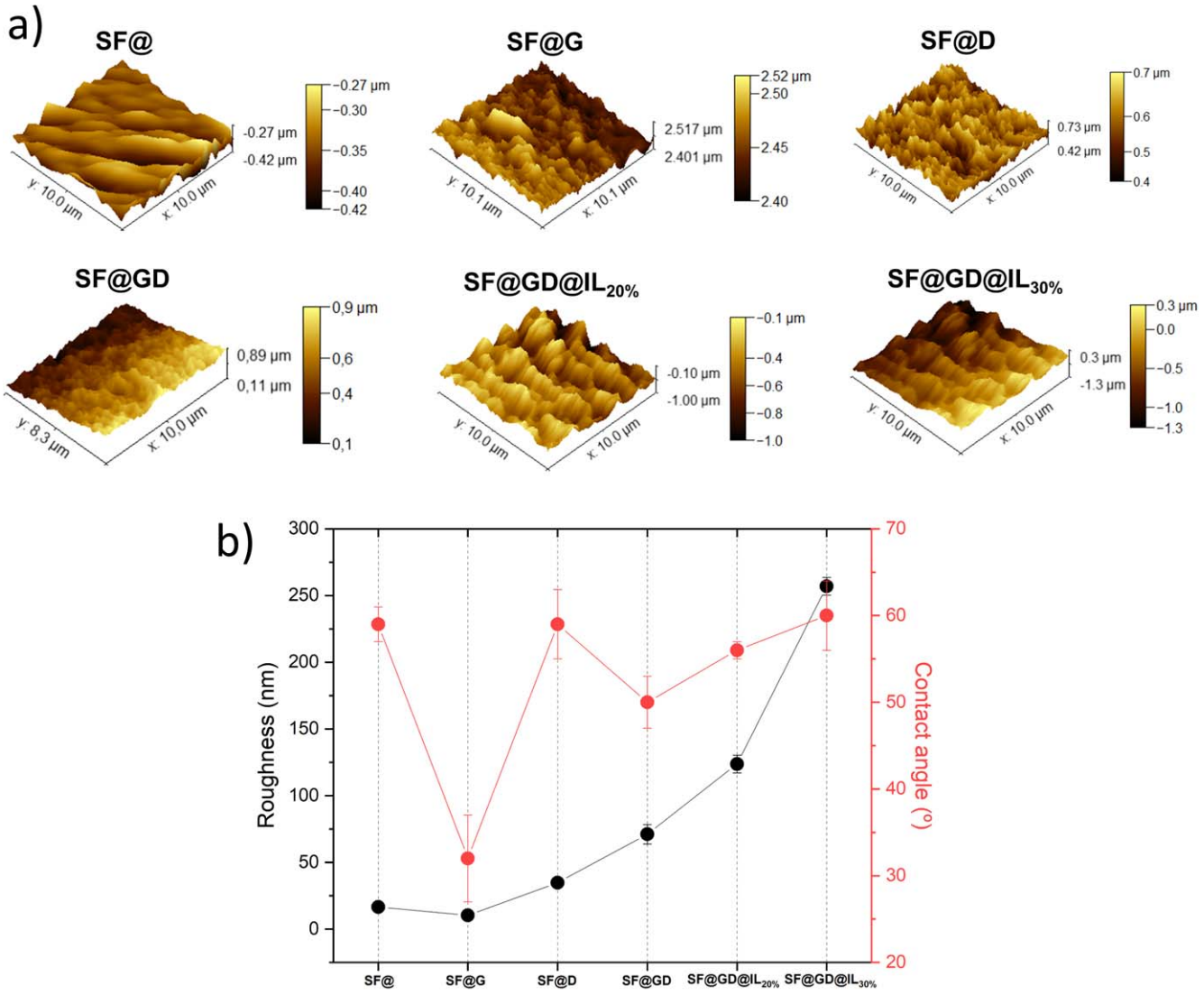


**Figure 4.** (a). AFM 3D images. (b). Mean roughness (left axis, black lines and symbols) and static water contact angle (right axis, red lines and symbols) of the SF-based electrolytes.

manifested in the wettability of the electrolytes. The water static CA values obtained for each sample are represented in Fig. 4b (right axis). SF@ exhibited a water CA of 59 ± 2° which dropped to 32 ± 5° in SF@G, presumably because of the significant hygroscopic nature of glycerol. The CA of SF@D (59 ± 4°) is, however, identical to that of SF@. In the case of the SF@GD material the CA value of 50 ± 3 demonstrates that the presence of DMSO helped increasing the low CA of SF@G. The inclusion of [Bmim]$PF_6$ further pushed the CA values up to the value of SF@ (Fig. 4b (right axis). The latter trend was expected, considering the hydrophobic character of [Bmim]$PF_6$. At this stage it is important to mention the study of Malali and Foloutan[51] on the wettability behaviour of [Bmim]$PF_6$ on a titania ($TiO_2$) surface. These authors demonstrated that a cation-rich layer was spread on the surface of $TiO_2$. The rings of the imidazolium cations were parallel to the surface, but in the upper layer they were almost vertical. Such positioning explained the wetting behaviour of this IL at the adjacent layer of surface and its non-wetting behaviour at long distances from the surface. The formation of this double layer[52] might also account for the increase of the CA value at increasing concentrations of [Bmim]$PF_6$ detected in the present study in the solid state.

The electrolytes were also examined by XRD with the goal of, not only getting information on the degree of order of the materials, but also detecting conformational changes promoted by the presence of the dopants on the SF chains. Prior to discussing these data, it is useful to emphasize that *Bombyx mori* silk exhibits three crystalline polymorphs, which are considered to be the main protein secondary structures: Silk I (a metastable state between a partially ordered α-helix and β-sheet structure), Silk II (antiparallel β-sheet structure characteristic of natural fibers) and Silk III (formed at air−liquid interfaces).[53] In the SF aqueous solution process preparation, the structural β-sheet sheets are first broken due to swelling, a process that is followed by disruption of the inter- and intramolecular hydrogen bonds between β-strands and anti-parallel β-sheets. The SF conformations of the regenerated (degummed) fibers are deeply influenced by the chemical environment surrounding the chains. Typically, during the formation of SF films from aqueous solutions, the arrangement of the protein crystalline blocks leads to one of the following situations: amorphous/random coils (disordered structure), Silk I or Silk II structures.[53,54]

The room temperature XRD patterns of SF@ (Fig. 5, black line) and SF@G (Fig. 5, red line) are practically identical. Both patterns exhibit two peaks of low intensity at 16.4 and 19.8°, which are attributed to the Silk I structure.[55,56] The XRD pattern of SF@ also gives rise to an ill-defined, very weak peak at 24.8° denoting the presence of a minor amount of Silk II structures (Fig. 5, black line). In the same $2\theta$ range the profiles of the XRD patterns of the SF@D, SF@GD and SF@GD@$IL_{20\%}$ electrolytes are dominated by a strong

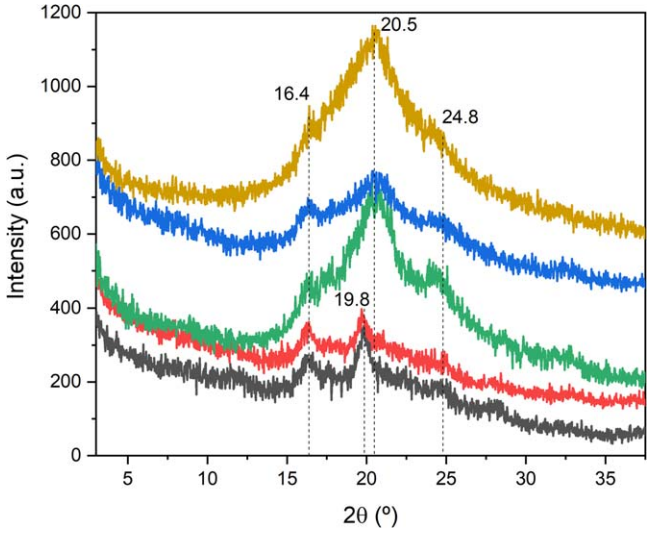


**Figure 5.** Room temperature XRD patterns of SF@ (black line), SF@G (red line), SF@D (green line), SF@GD (blue line) and SF@GD@$IL_{20\%}$ (yellow lines) electrolytes.

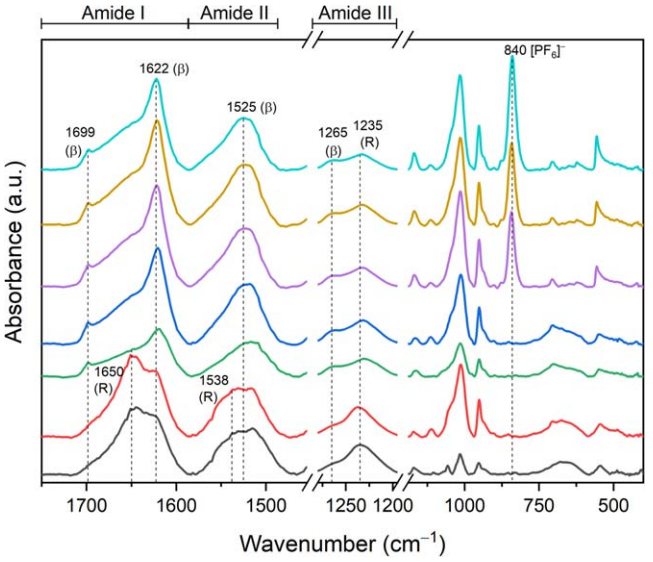


**Figure 6.** ATR/FT-IR spectra of the (a) SF@ (black line), (b) SF@G (red line), (c) SF@D (green line), (d) SF@GD (blue line), (e) SF@GD@$IL_{15\%}$, (violet line), (f) SF@GD@$IL_{20\%}$ (yellow line) and (g) SF@GD@$IL_{30\%}$ (cyanide line) electrolytes in the 1750–450 $cm^{-1}$ range.

band centered at 20.5° (Fig. 5, green, blue and yellow lines, respectively). Its large width arises from very limited coherent length. Two peaks are resolved in the band profiles at 16.4 and 24.8°. The shift of the 19.8° peak to 20.5° and the growth of the 24.8 ° peak in these three samples represent unequivocal evidences of the predominance of the Silk II structure.[55–63] This observation may be interpreted as a clear indication that the fraction of $\beta$-sheets in the SF@D, SF@GD and SF@GD@$IL_{20\%}$ electrolytes is considerably higher than in SF@ or SF@G. These findings confirm our claim that the increase of surface roughness of these three samples is related with the increase of the proportion of crystallinity.

Vibrational spectroscopy was used here, not only to identify the conformational state of the chains of SF in the electrolytes, but also to get insight into cation/anion interactions. Figure S4 shows the ATR/FT-IR spectra of the SF-based samples in the 4000–450 $cm^{-1}$ range. Such spectral information is of the utmost relevance, since the ionic conductivity is known to depend strongly on the proportion of amorphous material and on the degree of ionic association.

The inspection of the SF protein conformations relied on the examination of the Amide I, Amide II and Amide III vibration modes, because these modes, especially the former two modes, are very sensitive to the extent and strength of hydrogen bonding interactions.[53,64] Figure 6 shows SF characteristic bands associated with the vibration modes of the amide groups[65]: 1750–1585 $cm^{-1}$ (Amide I, which receives mainly the contribution of the C=O stretching vibration, but also those of the C–N stretching, and the C–C–N deformation vibrations), 1585–1485 $cm^{-1}$ (Amide II, which involves a mixed contribution of the N–H in-plane bending, C–N stretching, and C–C stretching vibrations), and 1285–1195 $cm^{-1}$ (Amide III, which involves the stretching vibration of the C–N group, coupled with NH deformation modes).

The SF@ sample produces in the Amide I region an intense band at 1650 $cm^{-1}$, due to a Silk I/random coil arrangement,[64,66,67] and another one, less intense, at 1622 $cm^{-1}$, attributed to Silk II conformations ($\beta$-sheets).[64,66,67] Thus, as expected, the non-doped SF film showed preferentially random coil conformations which coexisted with a minor proportion of $\beta$-sheet structures. Doping the SF film with glycerol (SF@G) did not affect this scenario, as indicated by the exact overlap between the profiles of the Amide I bands of SF@G and SF@. In contrast, the incorporation of DMSO into SF changed dramatically the shape of the Amide I band: (1) a new band emerged at 1699 $cm^{-1}$, associated with the $\beta$-sheet structures; (2) the band at 1622 $cm^{-1}$ (also due to $\beta$-sheet structures) got sharper; (3) the intensity of the 1650 $cm^{-1}$ band, characteristic of random coil conformations, was substantially reduced. The Amide I band of SF@GD is similar to that of SD@D, but the prominent band at 1622 $cm^{-1}$ became considerably stronger (cf relative intensity of the Amide I and Amide II bands in Fig. 6). The samples doped with $[Bmim]PF_6$ gave rise to Amide I bands that roughly did not differ from that produced by SF@GD, indicating that DMSO and $[Bmim]PF_6$ influenced in the same way the SF conformations.

The analysis of the Amide II and III bands yielded the same conclusions. For SF@ and SF@G the Amide II band is broad and displays a shoulder at 1538 $cm^{-1}$, ascribed to random coils. In contrast, for SF@D, SF@GD and SF@GD@$IL_x$ the band became sharper and its intensity maximum was shifted to 1525 $cm^{-1}$, a wavenumber typical of the $\beta$-sheet arrangement. In the case of the Amide III band, in spite of the fact that the maximum intensity for all samples was found at 1235 $cm^{-1}$, indicating the occurrence of random coils, a new band assigned to $\beta$-sheet arrangements emerged at 1265 $cm^{-1}$ in the ATR/FT-IR spectra of the samples doped with DMSO and $[Bmim]PF_6$.

The interactions between the $[Bmim]^+$ cation and the $PF_6^-$ anion, and between the cation and SF chains, can be examined on the basis of changes of intensity and frequency changes of characteristic bands.

Most of the vibrations associated with the butyl and propyl chains, and the imidazolium ring of $[Bmim]PF_6$ fall in the high frequency region (3200–2900 $cm^{-1}$).[68–71] In this spectral range, owing to the superposition of these bands with several strong bands of the samples lacking $[Bmim]PF_6$ (i.e., SF@, SF@G, and SF@D and SF@GD) (Fig. S5), it was only possible to discern in the ATR/FT-IR spectra of the SF@GD@$IL_x$ samples a band at 2965 $cm^{-1}$ and the growth of a shoulder at about 2918 $cm^{-1}$, assigned to the alkyl C−H stretching vibration of the butyl chain of $[Bmim]PF_6$.[68,69] Considering that $[Bmim]PF_6$ produces a band at 2940 $cm^{-1}$,[68,69,71] the marked downshift produced (to 2924–2918 $cm^{-1}$) by the SF@GD@$IL_x$ electrolytes is indicative of a strong interaction between the $Bmim^+$ cation and other components of the electrolyte.

The inspection of the 900–400 $cm^{-1}$ region of the ATR/FT-IR spectra is particularly useful. Marked spectral modifications resulted when $[Bmim]PF_6$ was added to the SF-based system. The most intense band seen at 840 $cm^{-1}$ (Fig. 6) is characteristic of the $\nu_3(T_{1u})$ mode of the "free" $PF_6^-$ ion.[70–72] The band at 877 $cm^{-1}$ (Fig. 7a) proves the formation of $[Bmim]^{+\cdots}PF_6^-$ contact ion pairs.[29] At lower wavenumbers further evidences of the coexistence of "free"

and coordinated $PF_6^-$ ions in the IL-doped electrolytes were found. The band observed at 766 $cm^{-1}$ (Fig. 7b) is associated with contact ion pairs[72] and those at 754 and 741 $cm^{-1}$ are attributed to "free" $PF_6^-$ species.[70–72]

The thermal properties of the SF-based electrolytes were studied by DSC. The corresponding thermograms are reproduced in Fig. 8a. The most relevant thermal data are given in Table SII.

The DSC curve of SF@ displays two endothermic events (Fig. 8a, black line). The very weak and broad event centered at about 69 °C (onset temperature ($T_{onset}$) = 38 °C and enthalpy ($\Delta H$) = −93 J $g^{-1}$) is associated with the release of water molecules present in the SF matrix. We recall that the preparation of the SF-based samples was performed in aqueous medium. The second endothermic event seen at higher temperatures ($T_{onset}$ = 259 °C, $T_{peak}$ = 281 °C and $\Delta H$ = −135 J $g^{-1}$) is attributed to the thermal degradation of the SF matrix.[73,74] The DSC curves of SF-based materials sometimes show the glass transition depression, crystallization and degradation peaks at characteristic temperatures.[73–76] None of these thermal events are visible in the present thermogram. In terms of thermal behaviour, SF@G does not differ significantly from the non-doped sample. This material produced the same pair of endotherms at low temperature ($T_{onset}$ = 66 °C, $T_{peak}$ = 67.3 °C and $\Delta H$ = −32.9 J $g^{-1}$) and high temperature ($T_{onset}$ = 258 °C, $T_{peak}$ = 281 °C and $\Delta H$ = −89.3 J $g^{-1}$). The existence of DMSO in the other electrolytes led, however, to dramatic changes in the DSC thermograms. This is not surprising considering that DMSO (boiling point of 189 °C) is a very hygroscopic solvent and that DMSO-containing materials may decompose at lower temperatures than pure DMSO.[77] An obvious increase of the area of the low-temperature endothermic peak observed for SF@ and SF@G resulted in all the samples where DMSO was present, mainly due to the release of the water molecules adsorbed to DMSO. A new endothermic peak with $T_{onset}$ > 111 °C and a $T_{peak}$ between 133 °C (SF@D) and 155 °C (SF@GD@$IL_{30\%}$) emerged as well. The $T_{peak}$ and $\Delta H$ increased in the order SF@D < SF@GD < SF@GD@$IL_{15\%}$ < SF@GD@$IL_{20\%}$ < SF@GD@$IL_{30}$, suggesting that the increase of the number of dopants and of the IL concentration enhanced this event. The latter endotherm is attributed to the evaporation of DMSO. The DSC curves of the [Bmim]$PF_6$-doped electrolytes exhibit in addition a very weak exothermic event located at 219 °C (SF@GD@$IL_{15\%}$) and 230 °C (SF@GD@$IL_{30\%}$) indicative of $\beta$-sheet crystallization. The ATR/FT-IR and XRD data discussed above demonstrated that the electrolytes doped with IL adopted mainly Silk II ($\beta$-sheet) conformations. For this reason, the DSC exotherm attributed to $\beta$-sheet crystallization is easily detected in these samples. Accordingly, the increase of IL concentration led to an increase of the $\Delta H$ of crystallization (Table SII).

The thermal stability of SF@ and [Bmim]$PF_6$ is quite high: up to about 220 °C (Fig. 8b, black line) and 350 °C,[78] respectively. Close examination of the TGA curves shown in Fig. 8b reveals that in the three IL-doped electrolytes the weight losses occurring below 200 °C involved essentially the release of adsorbed water and DMSO, corroborating the DSC data. Beyond this temperature, the curves resembled closely that of SF@. For samples lacking the IL and including glycerol (S@G (Fig. 8b, red line) and SF@GD (Fig. 8b, blue line), thermal degradation occurred at a regular pace below 300 °C.

Impedance spectroscopy was used to evaluate the ionic conductivity of the SF-based electrolytes (Fig. 9 and Figs. S6–S11). Figure 9 demonstrates that over the whole range of temperatures analyzed, the ionic conductivity values of the [Bmim]$PF_6$-containing electrolytes (Fig. 9, violet, yellow and cyanide lines) are about four orders of magnitude higher than that of SF@G (Fig. 9, red line), and two orders of magnitude higher than those of SF@D (Fig. 9, green line) and SF@GD (Fig. 9, blue line). In the case of the samples lacking [Bmim]$PF_6$ (i.e., SF@G, SF@D and SF@GD) it is clear that the addition of DMSO boosted the ionic conductivity. The sample that exhibited the highest ionic conductivity of the whole series studied was SF@GD@$IL_{30\%}$ (1.07 and 4.61 mS $cm^{-1}$, at 22 and 100 °C, respectively), indicating that a marked benefit resulted from the incorporation of the IL in the electrolyte formulation. Ionic conduction is promoted by ILs through the increase of charge carriers and of the amorphous phase content in the doped electrolytes. Besides the increase of mobile charge carriers, the addition of [Bmim]$PF_6$ also possibly stimulated a better separation of the SF chains, resulting in their more pronounced movements and consequent increase of ionic conductivity. Given the high complexity of the electrolyte samples, it is difficult to exactly identify the charge carriers responsible for ion conduction. Apart from the $[Bmim]^+$ cations and the $PF_6^-$anions, it is clear that protons, originating from adsorbed water molecules, also contributed, via Grotthuss or vehicular mechanisms, to the conductivity values measured. It is worth emphasizing that the levels of ionic conductivity found in the present case are of the same order of magnitude or even higher than those reported for the most recently introduced high-performance standard or natural-based solid electrolytes.[79–82]

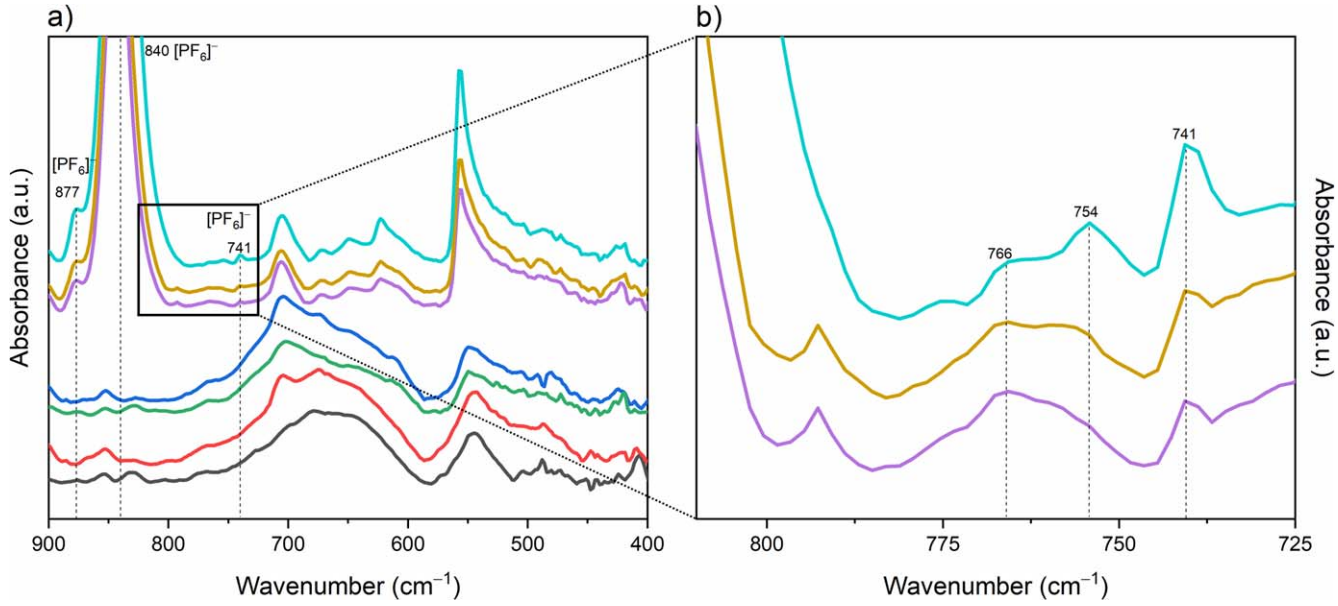


**Figure 7.** ATR/FT-IR spectra of the SF@ (black line), SF@G (red line), SF@D (green line), SF@GD (blue line), SF@GD@$IL_{15\%}$, (violet line), SF@GD@$IL_{20\%}$ (yellow line) and SF@GD@$IL_{30\%}$ (cyanide line) electrolytes in the (a) 900–400 $cm^{-1}$ and (b) 850–725 $cm^{-1}$ ranges.

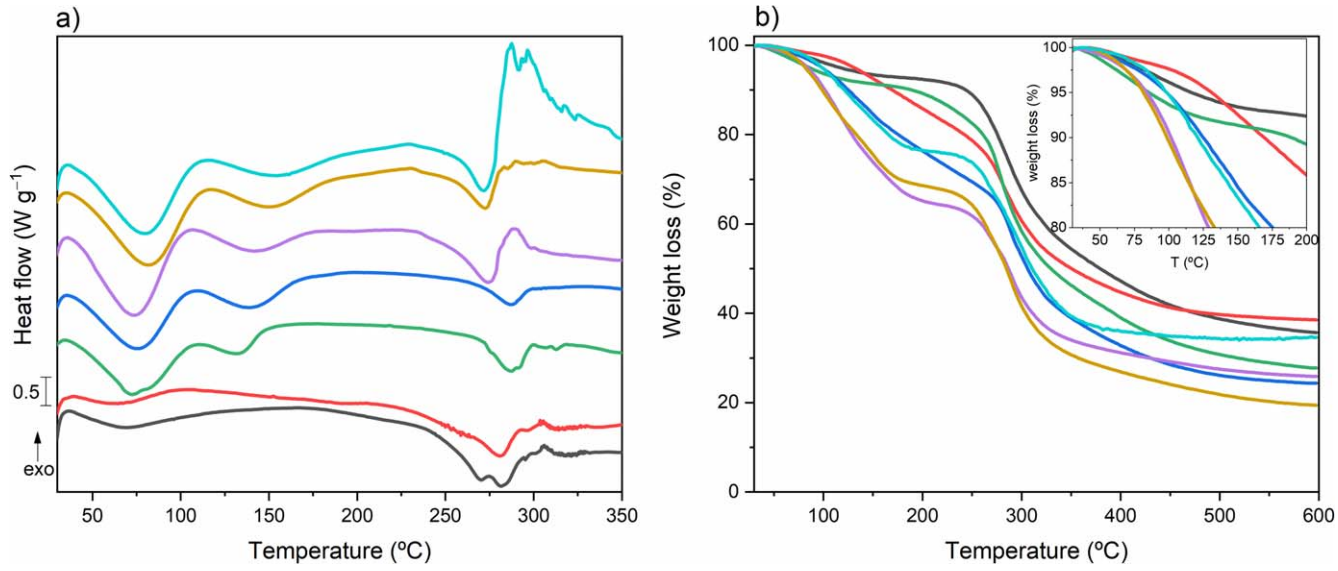


**Figure 8.** DSC (a) and TGA (b) curves of SF@ (black line), SF@G (red line), SF@D (green line), SF@GD (blue line), SF@GD@IL$_{15\%}$, (violet line), SF@GD@IL$_{20\%}$ (yellow line) and SF@GD@IL$_{30\%}$ (cyanide line) electrolytes.

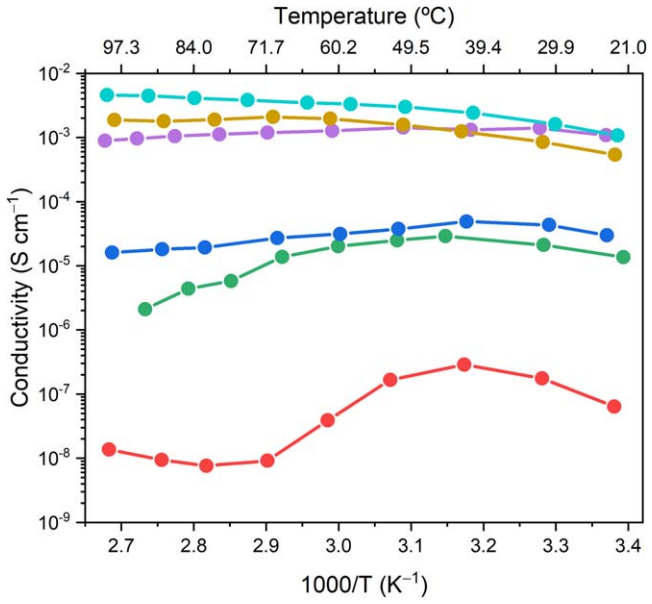


**Figure 9.** Arrhenius conductivity plot of the SF@G (red line), SF@D (green line), SF@GD (blue line), SF@GD@IL$_{15\%}$, (violet line), SF@GD@IL$_{20\%}$ (yellow line) and SF@GD@IL$_{30\%}$ (cyanide line) electrolytes. The lines are just guides for the eyes.

In the case of the SF@G electrolyte, the conductivity increased with the increase of temperature reaching a maximum at about 43 °C, but then it decreased reaching a minimum at about 70 °C; beyond this temperature it remained practically unchanged (Fig. 9, red line). An effect similar to this was found in SF@D (Fig. 9, green line) and SF@GD (Fig. 9, blue line), but the decrease was considerably less pronounced that in SF@G. This rather unusual behavior leads us to suppose that in both these samples something occurred in the 40 °C–70 °C temperature range. The SF@GD@IL$_{20\%}$ and SF@GD@IL$_{30\%}$ materials exhibited non-linear variations of ionic conductivity with temperature (Fig. 9, yellow and cyanide lines, respectively), which may be described by the Vogel-Tammann-Fulcher (VTF) equation. However, it is noteworthy that these variations are very small indeed. In fact, for SF@GD@IL$_{15\%}$ the ionic conductivity remained practically constant (Fig. 9, violet line).

To determine if temperature-dependent structural modifications of the electrolytes could justify the anomalous effect detected in the Arrhenius conductivity plot of SF@, SF@G and SF@GD, we recorded the XRD patterns of selected electrolytes (SF@GD and SF@GD@IL$_{20\%}$) during heating between 25 and 100 °C (Fig. 10), and after cooling down to room temperature.

Upon increasing the temperature of SF@GD a decrease of intensity of the 12.3 and 16.4° peaks of the XRD pattern occurred (Fig. 10a). Both these peaks are assigned to Silk I conformations.[55,56,61] In parallel the 20.2° peak, assigned to Silk II conformations,[61–63] became weaker and was shifted to 20.7° (Fig. 10a). These findings confirm the claim that temperature affected the structural organization of this electrolyte. Moreover, the changes indicated were detected above 45 °C–55 °C and this is precisely the temperature range that induced the ionic conductivity drop. We may assume that SF@, SF@G and SF@D underwent similar structural changes. In a previous work of some of us,[24] involving SF-based electrolytes for application in electrochromic devices, we reported similar perturbations in the ionic conductivity behavior of the electrolytes with the increase of temperature.

Figure 10b reveals that the temperature increase did not change the profile of the XRD patterns of SF@GD@IL$_{20\%}$. This result points out that the addition of [Bmim]PF$_6$ to SF had a very effective stabilizing effect on the structural organization of the electrolytes which was visibly not affected by temperature variations.

Figure 11 depicts the room temperature microelectrode cyclic voltammograms of selected electrolytes over the −2.0 to 6.0 V range. CV curves for other samples are given in Fig. S12.

The SF@GD@IL$_x$ electrolytes exhibited very low reduction and oxidation currents (<3.0 nA), a proof that the samples are sufficiently stable at the voltage interval studied.[83]

## Conclusions

In the quest for advanced new electrolytes for future energy-efficient devices, respecting the *Sustainable Development Goals*, green *Bombyx mori* SF-based electrolytes exhibiting high ionic conductivity were synthesized for the first time via the incorporation of glycerol, DMSO and [Bmim]PF$_6$ into the natural protein macromolecule matrix. The electrolytes were obtained as high quality, transparent, homogenous films displaying excellent mechanical properties.

The effect of DMSO and [Bmim]PF$_6$ on the conformational organization of the SF chains was found to be similar, both dopants

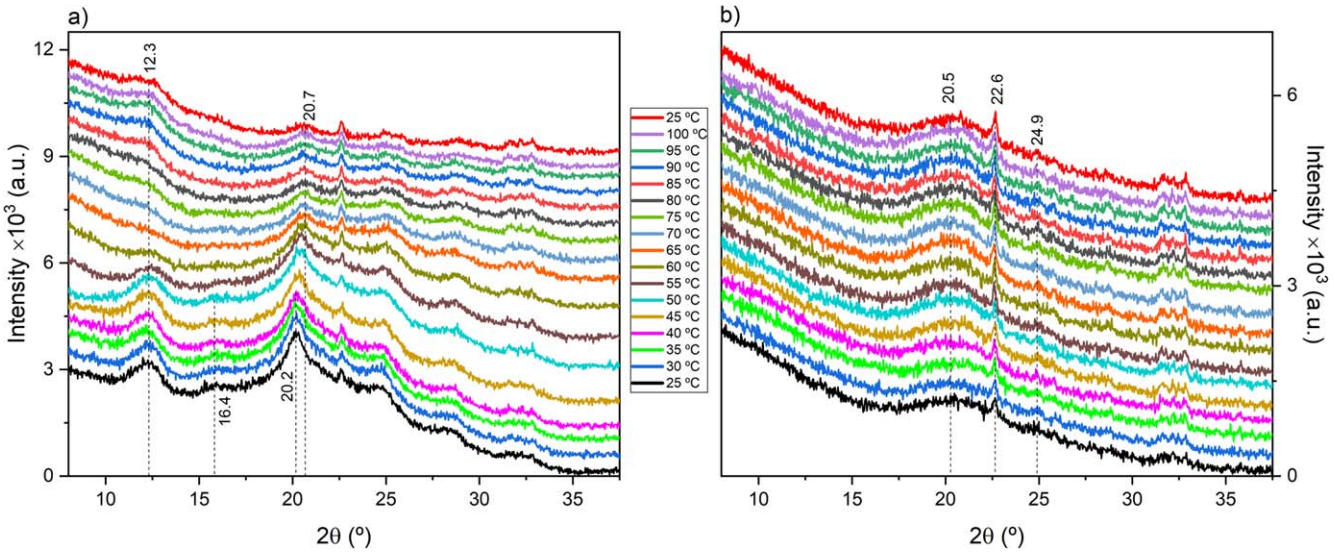


**Figure 10.** XRD patterns of the (a) SF@GD and (b) SF@GD@$IL_{20\%}$ electrolytes as a function of temperature.

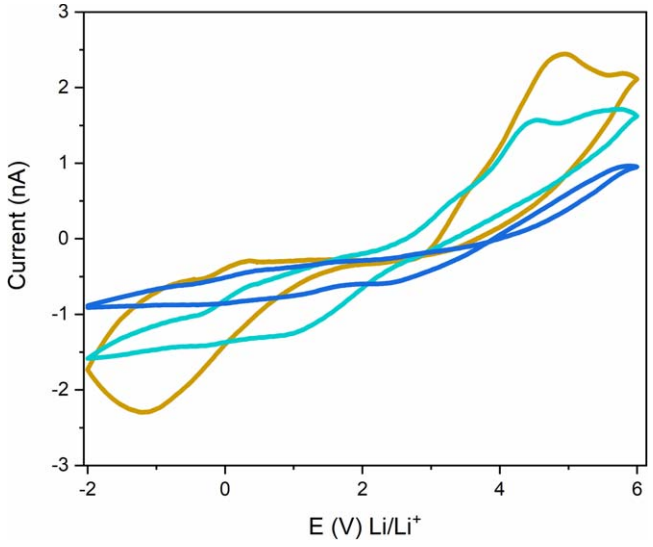


**Figure 11.** Cyclic voltammetry curves of the SF@GD (blue line), SF@GD@$IL_{20\%}$ (yellow line) and SF@GD@$IL_{30\%}$ (cyanide line) electrolytes (scan rate of 500 mV $s^{-1}$).

inducing an increase of the fraction of ordered domain ($\beta$-sheets). In the absence of [Bmim]$PF_6$, the increase of temperature caused, however, marked structural changes of the SF chains. Apart from acting as solvent of [Bmim]$PF_6$, DMSO promoted the increase of the ionic conductivity of the electrolytes and of the average roughness.

In the whole range of temperatures examined the highest ionic conductivity was exhibited for the sample including 30% wt. of [Bmim]$PF_6$ (1.07 and 4.61 mS $cm^{-1}$, at 22 and 100 °C, respectively), being two orders of magnitude higher than those of the electrolytes lacking IL. In the IL-doped electrolytes "free" and coordinated anions were detected.

In spite of the high number of additives, the thermal stability of the electrolytes remained similar to that of SF itself (up to 200 °C). Below this temperature, the release of the occluded solvents took place.

The present results are very encouraging and clearly justify further investigation. This work opens new avenues for the development of cleaner, safer, cheaper and more sustainable energy materials.

## Acknowledgments

Verónica de Zea Bermudez would like to express her gratitude to Professor Michel Armand who, during her PhD thesis at Grenoble (1989–1992), was an endless source of ideas that made her work productive and stimulating. His qualities, as an inspiring and extraordinary scientist, equal his kindness, generosity and great heart. This work was supported by National funds by Foundation for Science and Technology (FCT) in the framework of the Strategic Funding UID/QUI/00686/2018, UID/QUI/00686/2019, UID/QUI/50006/2019 and UID/QUI/00313/2020. The authors thank FEDER funds through the COMPETE 2020 Program and National Funds through FCT under the projects PEst-OE/QUI/UI0616/2014, LUMECD (POCI-01-0145-FEDER-016884 and PTDC/CTM-NAN/0956/2014), UniRCell (POCI-01-0145-FEDER-016422 and SAICTPAC/0032/2015), PORPLANTSURF (POCI-01-0145-FEDER-029785 and PTDC/CTM-REF/29785/2017), and NORTE-01-0145-FEDER-030858. R.F.P.P thanks FCT-UM for the researcher contract in the scope of Decreto-Lei 57/2016 and 57/2017. H.M.R. Gonçalves was funded by PTDC/BTM-MAT/30858/2017.

## ORCID

Helena M. R. Rodrigues https://orcid.org/0000-0001-6210-8736
Filipe A. A. Paz https://orcid.org/0000-0003-2051-5645
Joana F. M. Sousa https://orcid.org/0000-0002-2852-4143
Artur J. M. Valente https://orcid.org/0000-0002-4612-7686
Maria M. Silva https://orcid.org/0000-0002-5230-639X
Verónica de Zea Bermudez https://orcid.org/0000-0002-7577-4938
Rui F. P. Pereira https://orcid.org/0000-0001-7279-5728

## References

1. M. B. Armand, J. M. Chabagno, and M. Duclot, *Second International Meeting on Solid Electrolytes*, ed. U. O. S. Andrews (St. Andrews, Scotland) p. 651 (1978).
2. M. B. Armand, J. M. Chabagno, and M. J. Duclot, *Fast Ion Transport in Solids*, ed. P. Vashita, J. N. Mundy, and G. K. Shenoy (Elsevier, Amsterdam) p. 131 (1979).
3. H. Zhang et al., *Angew. Chem. Int. Ed.*, **59**, 534 (2020).
4. L. Meabe, N. Goujon, C. Li, M. Armand, M. Forsyth, and D. Mecerreyes, *Batteries & Supercaps*, **3**, 68 (2020).
5. J. M. Tarascon and M. Armand, *Nature*, **414**, 359 (2001).
6. P. Yao, H. Yu, Z. Ding, Y. Liu, J. Lu, M. Lavorgna, J. Wu, and X. Liu, *Front. Chem.*, **7** (2019).
7. M. Armand, F. Endres, D. R. MacFarlane, H. Ohno, and B. Scrosati, *Nat. Mater.*, **8**, 621 (2009).
8. G. Gebresilassie Eshetu, M. Armand, B. Scrosati, and S. Passerini, *Angew. Chem. Int. Ed.*, **53**, 13342 (2014).

9. UNESCO, "UNESCO moving forward the 2030 agenda for sustainable development: Sustainable development goals." https://en.unesco.org/creativity/files/unesco-moving-forward-2030-agenda-sustainable (2017).
10. V. L. Finkenstadt, *Appl. Microbiol. Biotechnol.*, **67**, 735 (2005).
11. M. F. Shukur and M. F. Z. Kadir, *Ionics*, **21**, 111 (2015).
12. T. D. O. Gadim, A. G. P. R. Figueiredo, N. C. Rosero-Navarro, C. Vilela, J. A. F. Gamelas, A. Barros-Timmons, C. P. Neto, A. J. D. Silvestre, C. S. R. Freire, and F. M. L. Figueiredo, *ACS Appl. Mater. Interfaces*, **6**, 7864 (2014).
13. T. D. O. Gadim, F. J. A. Loureiro, C. Vilela, N. Rosero-Navarro, A. J. D. Silvestre, C. S. R. Freire, and F. M. L. Figueiredo, *Electrochim. Acta*, **233**, 52 (2017).
14. R. D. Alves, L. C. Rodrigues, J. R. Andrade, A. Pawlicka, L. Pereira, R. Martins, E. Fortunato, and M. M. Silva, *Mol. Cryst. Liquid Cryst.*, **570**, 1 (2013).
15. E. Raphael, C. O. Avellaneda, B. Manzolli, and A. Pawlicka, *Electrochim. Acta*, **55**, 1455 (2010).
16. N. N. Mobarak, N. Ramli, A. Ahmad, and M. Y. A. Rahman, *Solid State Ion.*, **224**, 51 (2012).
17. F. Bella, N. N. Mobarak, F. N. Jumaah, and A. Ahmad, *Electrochim. Acta,*, **151**, 306 (2015).
18. S. C. Nunes, R. F. P. Pereira, N. Sousa, M. M. Silva, P. Almeida, F. M. L. Figueiredo, and V. de Zea Bermudez, *Adv. Sustainable Syst.*, **1**, 1700070-n/a (2017).
19. F. M. Santos, P. C. Barbosa, R. F. P. Pereira, M. M. Silva, H. M. R. Gonçalves, S. C. Nunes, F. L. Figueiredo, A. J. M. Valente, and V. de Zea Bermudez, *Eur. Polym. J.*, **124**, 109453 (2020).
20. R. Leones et al., *J. Nanosci. Nanotechnol.*, **14**, 6685 (2014).
21. R. Ramadan, H. Kamal, H. M. Hashem, and K. Abdel-Hady, *Sol. Energ. Mat. Sol. Cells*, **127**, 147 (2014).
22. C. O. Avellaneda, D. F. Vieira, A. Al-Kahlout, S. Heusing, E. R. Leite, A. Pawlicka, and M. A. Aegerter, *Sol. Energ. Mat. Sol. Cells*, **92**, 228 (2008).
23. R. F. P. Pereira, M. M. Silva, and V. de Zea Bermudez, *Macromol. Mater. Eng.*, **300**, 1171 (2015).
24. R. F. P. Pereira, F. Sentanin, A. Pawlicka, M. C. Gonçalves, M. M. Silva, and V. de Zea Bermudez, *Chem. Electro. Chem.*, **3**, 1084 (2016).
25. I. S. Romero, N. P. Bradshaw, J. D. Larson, S. Y. Severt, S. J. Roberts, M. L. Schiller, J. M. Leger, and A. R. Murphy, *Adv. Funct. Mater.*, **24**, 3866 (2014).
26. J. Hou, C. Cao, F. Idrees, and X. Ma, *ACS Nano*, **9**, 2556 (2015).
27. X. Jia, C. Wang, C. Zhao, Y. Ge, and G. G. Wallace, *Adv. Funct. Mater.*, **26**, 1454 (2016).
28. X. Jia, C. Wang, V. Ranganathan, B. Napier, C. Yu, Y. Chao, M. Forsyth, F. G. Omenetto, D. R. MacFarlane, and G. G. Wallace, *ACS Energy Lett.*, **2**, 831 (2017).
29. R. F. P. Pereira, R. Gonçalves, M. Fernandes, C. M. Costa, M. M. Silva, V. de Zea Bermudez, and S. Lanceros-Mendez, *Adv. Sustainable Syst.*, **2**, 1800098 (2018).
30. R. F. P. Pereira, R. Brito-Pereira, R. Gonçalves, M. P. Silva, C. M. Costa, M. M. Silva, V. de Zea Bermudez, and S. Lanceros-Méndez, *ACS Appl. Mater. Interfaces*, **10**, 5385 (2018).
31. D. N. Rockwood, R. C. Preda, T. Yucel, X. Wang, M. L. Lovett, and D. L. Kaplan, *Nat. Protocols*, **6**, 1612 (2011).
32. H. Tao, D. L. Kaplan, and F. G. Omenetto, *Adv. Mater.*, **24**, 2824 (2012).
33. R. Hagiwara and Y. Ito, *J. Fluor. Chem.*, **105**, 221 (2000).
34. R. Milotskyi, L. Szabó, K. Takahashi, and C. Bliard, *Front. Chem.*, **7** (2019).
35. F. Cataldo, *Eur. Chem. Bull.*, **4**, 92 (2015).
36. M. Morita, F. Tachihara, and Y. Matsuda, *Electrochim. Acta*, **32**, 299 (1987).
37. A. Lewandowski and I. Majchrzak, *Electrochim. Acta,*, **42**, 267 (1997).
38. A. K. Srivastava and S. L. Shankar, *J. Chem. Eng. Data,*, **43**, 25 (1998).
39. B. Sun, X. Huang, S. Chen, J. Zhang, and G. Wang, *RSC Adv.*, **4**, 11115 (2014).
40. S. L. Agrawal and N. Rai, *J. Nanomater.*, **2015**, 1 (2015).
41. S. A. Kirillov, M. I. Gorobets, D. O. Tretyakov, M. B. Ataev, and M. M. Gafurov, *J. Mol. Liq.*, **205**, 78 (2015).
42. C. J. Bondue, M. Hegemann, C. Molls, E. Thome, and H. Baltruschat, *J. Electrochem. Soc.*, **163**, A1765 (2016).
43. P. K. R. Kottam, D. Kalkan, M. Wohlfahrt-Mehrens, and M. Marinaro, *J. Electrochem. Soc.*, **166**, A1574 (2019).
44. S. Hosseini, A. Abbasi, L.-O. Uginet, N. Haustraete, S. Praserthdam, T. Yonezawa, and S. Kheawhom, *Sci. Rep.*, **9**, 14958 (2019).
45. G. Kim, T. Liu, I. Temprano, E. A. Petrucco, N. S. Barrow, and C. P. Grey, *Johnson Matthey Technol. Rev.*, **62**, 332 (2018).
46. A. Sionkowska and A. Planecka, *Polym. Degrad. Stabil.*, **96**, 523 (2011).
47. C. S. Shivananda, R. Madhu Kumar, B. Narayana, K. Byrappa, P. Renu, Y. Wang, and Y. Sangappa, *Mater. Res. Innov.*, **21**, 210 (2016).
48. W. I. Abdel-Fattah, N. Atwa, and G. W. Ali, *Prog. Biomater.*, **4**, 77 (2015).
49. H. Zhang, L. Deng, M. Yang, S. Min, L. Yang, and L. Zhu, *Int. J. Mol. Sci.*, **12**, 3170 (2011).
50. C. Geão, A. R. Costa-Pinto, C. Cunha-Reis, V. P. Ribeiro, S. Vieira, J. M. Oliveira, R. L. Reis, and A. L. Oliveira, *J. Mater. Sci., Mater. Med.*, **30**, 27 (2019).
51. S. Malali and M. Foroutan, *J. Phys. Chem. C*, **121**, 11226 (2017).
52. M. Sha, G. Wu, Q. Dou, Z. Tang, and H. Fang, *Langmuir*, **26**, 12667 (2010).
53. M. McGill, G. P. Holland, and D. L. Kaplan, *Macromol. Rapid Commun.*, **40**, 1800390 (2019).
54. T. Asakura, Y. Suzuki, Y. Nakazawa, K. Yazawa, G. P. Holland, and J. L. Yarger, *Prog. Nucl. Magn. Reson. Spectrosc.*, **69**, 23 (2013).
55. H. Zhang, L.-L. Li, F.-Y. Dai, H.-H. Zhang, B. Ni, W. Zhou, X. Yang, and Y.-Z. Wu, *J. Transl. Med.*, **10**, 117 (2012).
56. S. Mobini, B. Hoyer, M. Solati-Hashjin, A. Lode, N. Nosoudi, A. Samadikuchaksaraei, and M. Gelinsky, *J. Biomed. Mater. Res. Part A*, **101A**, 2392 (2013).
57. R. Nazarov, H.-J. Jin, and D. L. Kaplan, *Biomacromolecules*, **5**, 718 (2004).
58. P. A. L. Lima, C. X. Resende, G. D. de Almeida Soares, K. Anselme, and L. E. Almeida, *Mater. Sci. Eng. C*, **33**, 3389 (2013).
59. U.-J. Kim, J. Park, H. Joo Kim, M. Wada, and D. L. Kaplan, *Biomaterials*, **26**, 2775 (2005).
60. C. Jiang, X. Wang, R. Gunawidjaja, Y. H. Lin, M. K. Gupta, D. L. Kaplan, R. R. Naik, and V. V. Tsukruk, *Adv. Funct. Mater.*, **17**, 2229 (2007).
61. H.-J. Jin and D. L. Kaplan, *Nature*, **424**, 1057 (2003).
62. L.-P. Yan, J. M. Oliveira, A. L. Oliveira, S. G. Caridade, J. F. Mano, and R. L. Reis, *Acta Biomater.*, **8**, 289 (2012).
63. C. Du, J. Jin, Y. Li, X. Kong, K. Wei, and J. Yao, *Mater. Sci. Eng. C*, **29**, 62 (2009).
64. D. J. Belton, R. Plowright, D. L. Kaplan, and C. C. Perry, *Acta Biomater.*, **73**, 355 (2018).
65. V. de Zea Bermudez, L. D. Carlos, and L. Alcácer, *Chem. Mat.*, **11**, 569 (1999).
66. X. Hu, D. Kaplan, and P. Cebe, *Macromolecules*, **39**, 6161 (2006).
67. A. Barth, *Biochim. Biophys. Acta, Bioenerg.*, **1767**, 1073 (2007).
68. S. Na, S. K. Chaurasia, R. K. Singh, and S. Chandra, *J. Phys. Chem. B*, **117**, 897 (2013).
69. Y. Gao, A. Voigt, M. Zhou, and K. Sundmacher, *Eur. J. Inorg. Chem.*, **2008**, 3769 (2008).
70. E. R. Talaty, S. Raja, V. J. Storhaug, A. Dölle, and W. R. Carper, *J. Phys. Chem. B*, **108**, 13177 (2004).
71. Y. U. Paulechka, G. J. Kabo, A. V. Blokhin, O. A. Vydrov, J. W. Magee, and M. Frenkel, *J. Chem. Eng. Data*, **48**, 457 (2003).
72. S. K. Chaurasia, R. K. Singh, and S. Chandra, *J. Polym. Sci. Pt. B-Polym. Phys.*, **49**, 291 (2011).
73. A. Motta, L. Fambri, and C. Migliaresi, *Macromol. Chem. Phys.*, **203**, 1658 (2002).
74. K. Yazawa, K. Ishida, H. Masunaga, T. Hikima, and K. Numata, *Biomacromolecules*, **17**, 1057 (2016).
75. N. Agarwal, D. A. Hoagland, and R. J. Farris, *J. Appl. Polym. Sci.*, **63**, 401 (1997).
76. X. Hu, D. Kaplan, and P. Cebe, *Macromolecules*, **41**, 3939 (2008).
77. T. T. Lam, T. Vickery, and L. Tuma, *J. Therm. Anal. Calorim.*, **85**, 25 (2006).
78. J. Seo, Y. L. Verma, M. P. Singh, and R. K. Singh, *J. Nanomater.*, **2012**, 1 (2012).
79. R. Chen, Q. Li, X. Yu, L. Chen, and H. Li, *Chem. Rev.* (2019).
80. W. Zhao, J. Yi, P. He, and H. Zhou, *Electrochem. Energy Rev.*, **2**, 574 (2019).
81. S. Choudhury, S. Stalin, D. Vu, A. Warren, Y. Deng, P. Biswal, and L. A. Archer, *Nat. Commun.*, **10**, 4398 (2019).
82. Y. N. Sudhakar, M. Selvakumar, and D. K. Bhat, *Biopolymer Electrolytes: Fundamentals and Applications in Energy Storage* (Elsevier, Amsterdam) p. 194 (2018).
83. G. Cheruvally et al., *J. Power Sources*, **172**, 863 (2007).